A crystal plasticity-based constitutive model for near-β titanium alloys under extreme loading conditions: Application to the Ti17 alloy

H.B. Boubaker [a,b,*], C. Mareau [a], Y. Ayed [a], G. Germain [a], A. Tidu [b]

[a] Arts et Métiers ParisTech, Campus d'Angers, LAMPA, 2 bd du Ronceray, 49035 Angers Cedex 1, France
[b] Laboratoire d'Étude des Microstructures et de Mécaniques des Matériaux (LEM3), CNRS Université de Lorraine, 57078 Metz cedex 03, France

Keywords:
Thermodynamics
Crystal plasticity
Finite strain
Ductile damage
β titanium alloys

A B S T R A C T

A crystal plasticity-based constitutive model is proposed to describe the thermo-mechanical behavior of the Ti17 titanium alloy subjected to extreme loading conditions. The model explicitly incorporates the effect of the crystallographic orientation of the hcp α and bcc β phases. The constitutive equations are built in the context of continuum thermodynamics with internal variables. The general framework of continuum damage mechanics is used to consider the impact of ductile damage on the mechanical behavior. The proposed model is implemented in a finite element method solver. The material parameters are identified from an extensive experimental dataset with an inverse method. According to the results, the impact of the strain rate and the temperature on the mechanical behavior is correctly depicted. The model is then used to evaluate the impact of temperature on strain localization. The role of the local texture on the development of ductile damage is also discussed for different specimen geometries. Finally, the impact of heat exchanges on the mechanical behavior at low and high temperatures is investigated.

1. Introduction

Due to their high strength-to-weight ratio, β-titanium alloys are largely used as structural materials for aerospace applications (Boyer and Briggs, 2005; Arrazola et al., 2009). This group of titanium alloys is interesting for aerospace applications owing to their high ultimate strength with a high fracture strain Weiss and Semiatin (1998, 1999), Kolli and Devaraj (2018). During fabrication operations, titanium alloys are subjected to severe loading conditions, namely high temperatures (higher than 1000 °C (de Buruaga et al., 2018)), high strain rates (around 10^5 s^{-1} (Thimm et al., 2021)) and large strains (Abukhshim et al., 2006; Wu and To, 2015; Childs et al., 2018). The thermo-mechanical behavior of titanium alloys under such conditions is quite complex, mostly because many metallurgical phenomena may impact microstructure development. For instance, some experimental studies have discussed the role of crystallographic slip on texture development (Dawson et al., 1998), the impact of recrystallization on the softening behavior (Momeni and Abbasi, 2010; Guo et al., 2019) or the consequences of strain localization (Semiatin et al., 1999).

For engineering purposes, numerical simulation is often used to determine the most appropriate processing conditions for β-titanium alloys (Baker, 2006; Zhang et al., 2007; Ye et al., 2013; Barbe et al., 2001). The robustness of such simulations is largely dependent on the accuracy of the associated set of constitutive relations. For severe loading conditions, the description of the mechanical behavior usually relies on empirical thermo-viscoplastic models (Johnson and Cook, 1983; Zerilli and Armstrong, 1987). For instance, the flow rule proposed by Johnson and Cook (1983) has been applied for the Ti6Al4V (Yaich et al., 2017; Harzallah et al., 2017), Ti17 (Ayed et al., 2016; Trabelsi et al., 2017) and Ti5553 (Wagner et al., 2020) alloys. Several modified Johnson–Cook flow rules have also been proposed to account for the softening behavior (Lee and Lin, 1998; Cai et al., 2015; Zhou et al., 2020) and the microstructural changes (Calamaz et al., 2008; Sima and Ozel, 2010) of β-titanium alloys. The model of Zerilli and Armstrong (1987) has been used by Cai et al. (2016) and Che et al. (2018) to describe the flow behavior of the Ti6Al4V alloy. A comparative study on the ability of the Johnson–Cook and the Zerilli–Armstrong models to predict the thermo-mechanical behavior of the Ti6554 β-titanium alloy has been performed by Zhan et al. (2014). According to the authors, while more experimental data is required to calibrate the Zerilli–Armstrong model, it provides a better description of strain softening when compared to the Johnson–Cook model.

While the aforementioned models account for the effect of temperature and strain rate on the mechanical behavior, they ignore the impact of microstructural heterogeneities. These models can therefore be referred to as macroscopic constitutive models in the sense that they

* Corresponding author at: Arts et Métiers ParisTech, Campus d'Angers, LAMPA, 2 bd du Ronceray, 49035 Angers Cedex 1, France.
E-mail address: houssemeddine.ben-boubaker@univ-lorraine.fr (H.B. Boubaker).

https://doi.org/10.1016/j.mechmat.2021.104198

represent the average response of the material of interest. However, when the characteristic length scale of the structure is similar to that of the microstructure, macroscopic constitutive models are inappropriate. This type of situation is commonly encountered for coarse-grained materials and/or processes with strong spatial localization (e.g. machining).

For metallic alloys, the general framework of crystal plasticity (Roters et al., 2010) provides a convenient method for incorporating the role of microstructural heterogeneities. While early theories (Mandel, 1973; Asaro, 1983) only considered the contribution of crystallographic slip to plastic deformation, some efforts have been made to include the effect of deformation twinning (Kalidindi, 1998; Salem et al., 2005; Abdolvand et al., 2020) and phase transformations (Turteltaub and Suiker, 2006; Suiker and Turteltaub, 2005). Such models have been used to investigate strain localization in a near-α titanium alloy (Bache et al., 2010) and in a $\alpha + \beta$ alloy (Kapoor et al., 2019). A crystal plasticity-based model was proposed by Kapoor et al. (2020) to investigate the effect of the orientation and the morphology of the α and β as well as their Burgers orientation relationship (BOR) on the deformation behavior of the Ti6Al4V alloy. A crystal plasticity-based model has been used by Goh et al. (2003) to study the effect of crystallographic orientation on the deformation response of Ti6Al4V alloy under fretting conditions. Furthermore, several studies have been performed using the framework of crystal plasticity to understand the effect of slip activity on low cycle fatigue behavior (Bridier et al., 2008, 2009; Farooq et al., 2020).

To deal with the degradation of mechanical properties, different options have been explored to couple damage mechanics with crystal plasticity, mostly in the context of fatigue damage (e.g. Aslan et al. (2011), Sabnis et al. (2016), Lindroos et al. (2019), Mareau (2020)) or ductile damage (e.g. Boudifa et al. (2009), Kim and Yoon (2015), Ling et al. (2016)). While the aforementioned approaches allow considering the impact of loading conditions, the role of temperature on damage development is often ignored.

In this work, a constitutive model is developed to describe the mechanical behavior of a coarse-grained Ti17 titanium alloy over a wide range of both temperatures and strain rates. This model considers not only the role of crystallographic slip but also that of damage on the mechanical behavior. For this purpose, the construction of constitutive relations relies on the crystal plasticity framework and continuum damage mechanics (Kachanov, 1958; Lemaitre et al., 1985; Chaboche, 2008; Bammann and Solanki, 2010). On the one hand, the crystal plasticity framework provides a convenient method for incorporating the contribution of crystallographic slip to plastic deformation. On the other hand, the introduction of a damage variable allows describing the impact of loading conditions (e.g. temperature, strain rate, loading direction) on ductile fracture. Also, because the Ti17 alloy displays a two- phase microstructure, a specific strategy, which relies on homogenization theory, is used to evaluate the contributions of individual variants to the mechanical behavior.

The present paper is organized as follows. The first section is dedicated to the description of the numerical model developed for the coarse-grained Ti17 titanium alloy. The strategy used to determine the corresponding material parameters is detailed in the second section. The experimental dataset used for parameter identification is also presented. Finally, the impact of loading conditions on microstructure development (crystallographic texture, strain localization) and ductile fracture is discussed in the final section.

2. Numerical model

2.1. Multiscale strategy

The Ti17 alloy (83%Ti, 5%Al, 2%Sn, 2%Zr, 4%Mo and 4%Cr) investigated in this study displays a microstructure consisting of 67% of lamellar α phase and 33% of equiaxed β phase. The corresponding microstructure, which is shown in Fig. 1, spans over multiple length scales. Specifically, while the average size of equiaxed β grains is about 1000 μm, the average thickness of α lamellae is around 0.8 μm.

Because of the multiple microstructural length scales, a multiscale strategy is proposed to model the mechanical behavior of the Ti17 alloy. On the one hand, β grains are directly represented through an *ad hoc* discretization procedure (see Fig. 2). On the other hand, due to their low thickness, it is not numerically conceivable to explicitly consider the role of α lamellae. To circumvent this difficulty, a homogenization strategy is used for the development of constitutive relations. Specifically, both the α and β phases are assumed to contribute to the mechanical behavior of a material point. As a result, according to the classical averaging relations of homogenization theory in the context of finite strains (Hill, 1967, 1972), the deformation gradient tensor $\boldsymbol{F}$ and the first Piola–Kirchoff stress tensor $\boldsymbol{P}$ are given for each material point by[1]:

$$\boldsymbol{F} = \zeta^{\beta}\boldsymbol{F}^{\beta} + \sum_{i}\zeta^{\alpha_i}\boldsymbol{F}^{\alpha_i} = \sum_{\phi}\zeta^{\phi}\boldsymbol{F}^{\phi} \tag{1}$$

$$\boldsymbol{P} = \zeta^{\beta}\boldsymbol{P}^{\beta} + \sum_{i}\zeta^{\alpha_i}\boldsymbol{P}^{\alpha_i} = \sum_{\phi}\zeta^{\phi}\boldsymbol{P}^{\phi} \tag{2}$$

According to the above relations, while multiple α phase variants may coexist (with volume fractions ζ^{α_i}), a single β phase variant (with volume fraction ζ^{β}) is considered for a given material point. The averaging relations do not allow uniquely specifying the deformation gradient tensor and the stress tensor associated with each variant. These relations must be supplemented with some constitutive equations and a localization rule. In the present work, a non-linear equivalent to the Voigt's assumption (Voigt, 1889) is adopted. This assumption leads to the simple localization rule:

$$\boldsymbol{F}^{\phi} = \boldsymbol{F} \tag{3}$$

It is worth mentioning that more realistic approximations, such as the laminate model Nemat-Nasser et al. (1996), can be used. However, because of the small size of α particles, this type of approach is not applicable here since a material point consists of multiple, rather than one single, α variants. Also, our attention is restricted to severe loading conditions, which involve high strain rates. For such conditions, phase transformations do not contribute to the deformation behavior. The volume fractions ζ^{ϕ} are therefore assumed to be constant during a deformation process. As a consequence, the specific power developed by internal forces p is given by:

$$p = \frac{1}{\rho}\boldsymbol{P} : \dot{\boldsymbol{F}} \tag{4}$$

$$= \sum_{\phi}\frac{\zeta^{\phi}}{\rho}\boldsymbol{P}^{\phi} : \dot{\boldsymbol{F}}^{\phi} \tag{5}$$

$$= \sum_{\phi}\zeta^{\phi}p^{\phi} \tag{6}$$

where ρ is the initial mass density.

In the context of thermomechanics, quantities such as the specific internal energy u and specific entropy s should be defined. Neglecting interfacial contributions, these thermodynamic quantities are obtained from:

$$u = \sum_{\phi}\zeta^{\phi}u^{\phi} \tag{7}$$

$$s = \sum_{\phi}\zeta^{\phi}s^{\phi} \tag{8}$$

In the following, adiabatic conditions are assumed. For this particular case, the specific dissipation source d is given by:

$$d = T\dot{s} \tag{9}$$

[1] Throughout this paper, the ϕ superscript is used to denote a quantity that is attached to either the β phase variant or one of the α phase variants (i.e. $\phi = \{\beta, \alpha_1, \alpha_2, \ldots\}$).

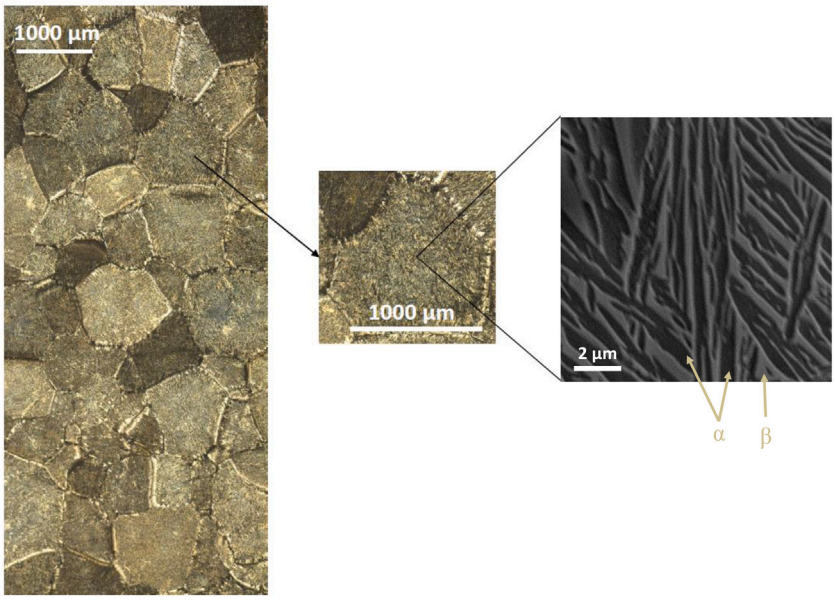

Fig. 1. Metallographic observations of the as-received $\alpha + \beta$ Ti17 titanium alloy.

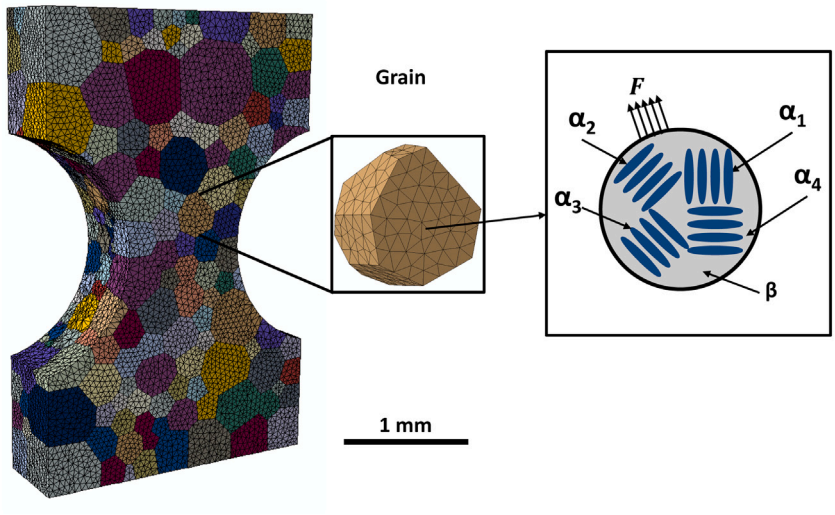

Fig. 2. Representation of the adopted modeling strategy of the $\alpha + \beta$ Ti17 microstructure.

$$= \sum_{\phi} \zeta^{\phi} \left(T \dot{s}^{\phi} \right) \tag{10}$$

$$= \sum_{\phi} \zeta^{\phi} d^{\phi} \tag{11}$$

The latter relation assumes that the temperature is the same for all the variants associated with a material point.

2.2. Constitutive equations

Kinematics. For each variant ϕ, the construction of constitutive relations relies on the multiplicative decomposition of the corresponding gradient tensor $\boldsymbol{F}^{\phi}$. Indeed, following the suggestion of Lee (1969), the deformation gradient tensor of a given variant is decomposed into thermoelastic (subscript *te*) and plastic (subscript *p*) contributions:

$$\boldsymbol{F}^{\phi} = \boldsymbol{F}_{te}^{\phi} \cdot \boldsymbol{F}_{p}^{\phi} \tag{12}$$

In the following, plastic flow is assumed to be incompressible so that $\det(\boldsymbol{F}_{p}^{\phi}) = 1$. Also, the above multiplicative decomposition allows identifying the thermoelastic and plastic contributions to the power developed by internal forces with:

$$p^{\phi} = \frac{1}{\rho} \boldsymbol{S}^{\phi} : \dot{\boldsymbol{E}}_{te}^{\phi} + \frac{1}{\rho} \boldsymbol{\Sigma}^{\phi} : \boldsymbol{L}_{p}^{\phi} \tag{13}$$

The thermoelastic strain tensor $\boldsymbol{E}_{te}^{\phi}$ is evaluated from the thermoelastic contribution to the deformation gradient tensors as follows:

$$\boldsymbol{E}_{te}^{\phi} = \frac{1}{2} \left(\left(\boldsymbol{F}_{te}^{\phi} \right)^{T} \cdot \boldsymbol{F}_{te}^{\phi} - \boldsymbol{1} \right) \tag{14}$$

The plastic contribution to the velocity gradient, which is denoted by $\boldsymbol{L}_{p}^{\phi}$, is obtained for each variant from:

$$\boldsymbol{L}_{p}^{\phi} = \dot{\boldsymbol{F}}_{p}^{\phi} \cdot \left(\boldsymbol{F}_{p}^{\phi} \right)^{-1} \tag{15}$$

Also, for each variant, the second Piola–Kirchoff stress tensor $\boldsymbol{S}^{\phi}$ is connected to the corresponding first Piola–Kirchoff stress tensor $\boldsymbol{P}^{\phi}$ according to:

$$\boldsymbol{S}^{\phi} = \left(\boldsymbol{F}_{te}^{\phi} \right)^{-1} \cdot \boldsymbol{P}^{\phi} \cdot \left(\boldsymbol{F}_{p}^{\phi} \right)^{T} \tag{16}$$

Table 1
State variables and associated thermodynamic forces used for the construction of constitutive relations.

	State variable	Thermodynamic force
Thermoelastic strain tensor	$\boldsymbol{E}_{te}^{\phi}$	$\boldsymbol{S}^{\phi}/\rho$
Absolute temperature	T	$-s^{\phi}$
Hardening variables	λ_s^{ϕ}	r_s^{ϕ}/ρ
Damage variable	D	$-Y^{\phi}/\rho$

In a similar fashion, the Mandel stress tensor $\boldsymbol{\Sigma}^{\phi}$, which is the power conjugate to the plastic part of the velocity gradient, is given by:

$$\boldsymbol{\Sigma}^{\phi} = \left(\boldsymbol{F}_{te}^{\phi}\right)^{T} \cdot \boldsymbol{P}^{\phi} \cdot \left(\boldsymbol{F}_{p}^{\phi}\right)^{T} \tag{17}$$

In the present work, plastic flow is the sole result of crystallographic slip. The framework of crystal plasticity (Roters et al., 2010) provides a convenient way of considering the role of crystallographic slip on the deformation behavior. For this purpose, a set of slip systems is associated with each variant. Each slip system s consists of a slip plane (with unit normal $\boldsymbol{n}_s^{\phi}$) and a slip direction (denoted by $\boldsymbol{m}_s^{\phi}$). Within this framework, the plastic contribution to the velocity gradient is obtained from:

$$\boldsymbol{L}_{p}^{\phi} = \sum_{s} \boldsymbol{m}_s^{\phi} \otimes \boldsymbol{n}_s^{\phi} \dot{\gamma}_s^{\phi} \tag{18}$$

where $\dot{\gamma}_s^{\phi}$ is the shear strain rate for the sth slip system.

State equations. The list of state variables used for the construction of constitutive equations is presented in Table 1. It consists of the thermoelastic strain tensor $\boldsymbol{E}_{te}^{\phi}$, the absolute temperature T, the damage variable D and a set of hardening variables. It is worth mentioning that, in a similar fashion to the temperature, the damage variable is the same for all variants. The underlying assumption is that the development of damage cannot be restricted to a single variant. The damage variable is therefore representative of the degradation of the mechanical properties of a material point, rather than that of a specific variant.

In the following, the hardening variable attached to the sth slip system is denoted by λ_s^{ϕ}. For a given slip system, the hardening variable λ_s^{ϕ} is connected to the corresponding dislocation density ϱ_s^{ϕ} with:

$$\lambda_s^{\phi} = b_s^{\phi}\sqrt{\varrho_s^{\phi}} \tag{19}$$

where b_s^{ϕ} is the norm of the Burgers vector.

For each variant, the specific free energy $a^{\phi} = u^{\phi} - s^{\phi}T$ is decomposed into thermoelastic, thermal and hardening contributions:

$$a^{\phi}[\boldsymbol{E}_{te}^{\phi}, T, D, \lambda_s^{\phi}] = a_{te}^{\phi}[\boldsymbol{E}_{te}^{\phi}, T, D] + a_{th}^{\phi}[T] + a_{hd}^{\phi}[T, D, \lambda_s^{\phi}] \tag{20}$$

According to the above decomposition, the present model assumes that, for each variant, the development of damage affects both the thermoelastic behavior and the hardening behavior. The thermoelastic contribution is given by:

$$\begin{aligned} a_{te}^{\phi} = {} & \frac{1}{2\rho}\boldsymbol{E}_{te}^{\phi} : \mathbb{C}^{\phi} : \boldsymbol{E}_{te}^{\phi} - \frac{1}{\rho}\boldsymbol{E}_{te}^{\phi} : \mathbb{C}^{\phi} : \boldsymbol{\alpha}^{\phi}\left(T - T_0\right) \\ & + \frac{1}{2\rho}\boldsymbol{\alpha}^{\phi} : \left(\mathbb{C}^{\phi} - \tilde{\mathbb{C}}^{\phi}\right) : \boldsymbol{\alpha}^{\phi}\left(T - T_0\right)^2 \end{aligned} \tag{21}$$

where $\mathbb{C}^{\phi}$ (respectively $\tilde{\mathbb{C}}^{\phi}$) is the current (respectively initial) stiffness tensor, $\boldsymbol{\alpha}^{\phi}$ is the thermal expansion tensor and T_0 is a reference temperature. While the current stiffness tensor $\mathbb{C}^{\phi}$ is impacted by both temperature and damage, the initial stiffness tensor $\tilde{\mathbb{C}}^{\phi}$ solely depends on temperature. Following the idea of Marigo (1991), the consideration of closure effects relies on the decomposition of the stiffness tensor into spherical and deviatoric contributions. Specifically, in the present work, the stiffness tensor $\mathbb{C}^{\phi}$ is calculated from the elastic strain tensor $\boldsymbol{E}_{e}^{\phi} = \boldsymbol{E}_{te}^{\phi} - \boldsymbol{\alpha}^{\phi}\left(T - T_0\right)$ with:

$$\mathbb{C}^{\phi} = \begin{cases} (1-D)\,\tilde{\mathbb{C}}^{\phi}, & \mathrm{tr}[\boldsymbol{E}_{e}^{\phi}] > 0 \\ (1-D)\,\tilde{\mathbb{C}}^{\phi} + D\mathbb{P}_s : \tilde{\mathbb{C}}^{\phi} : \mathbb{P}_s, & \mathrm{tr}[\boldsymbol{E}_{e}^{\phi}] \leq 0 \end{cases} \tag{22}$$

The spherical projection tensor $\mathbb{P}_s$ is given by:

$$\mathbb{P}_s = \frac{1}{3}\mathbf{1} \otimes \mathbf{1} \tag{23}$$

According to Eq. (22), when the spherical elastic strain is positive, stiffness properties are fully degraded for a damaged variant. However, due to closure effects, the spherical contribution to the stiffness tensor is recovered when the spherical elastic strain is negative.

For each variant, the thermal contribution a_{th} to the specific free energy is given by:

$$a_{th}^{\phi} = \tilde{c}_p\left(T - T_0 - T\ln\left[\frac{T}{T_0}\right]\right) \tag{24}$$

where $\tilde{c}_p$ is the initial specific heat capacity for the phases.

Finally, the contribution a_{hd}^{ϕ} allows considering the storage of energy associated with the formation of crystallographic defects (e.g. dislocations). This contribution depends on temperature, damage and hardening variables according to:

$$a_{hd}^{\phi} = \frac{1}{2\rho}H^{\phi}[T](1-D)\sum_{s}\lambda_s^{\phi}\sum_{t}h_{st}^{\phi}\lambda_t \tag{25}$$

In the above equation, H^{ϕ} is the temperature-dependent isotropic hardening modulus and h^{ϕ} is a matrix that allows considering the possible interactions between different slip systems. It should be noticed that the development of damage is associated with a softening phenomenon since the contribution of hardening variables to free energy vanishes for a fully damaged material point.

The differentiation of the specific free energy with respect to the thermoelastic strain tensor $\boldsymbol{E}_{te}^{\phi}$ leads to the state equation for the second Piola–Kirchhoff $\boldsymbol{S}^{\phi}$:

$$\boldsymbol{S}^{\phi} = \rho\frac{\partial a^{\phi}}{\partial \boldsymbol{E}_{te}^{\phi}} = \mathbb{C}^{\phi} : \left(\boldsymbol{E}_{te}^{\phi} - \boldsymbol{\alpha}^{\phi}\left(T - T_0\right)\right) \tag{26}$$

The specific entropy s^{ϕ} for each variant is obtained from the differentiation of the specific free energy with respect to the absolute temperature:

$$\begin{aligned} s^{\phi} = {} & -\frac{\partial a^{\phi}}{\partial T} = -\frac{1}{2\rho}\boldsymbol{E}_{te}^{\phi} : \frac{\partial \mathbb{C}^{\phi}}{\partial T} : \boldsymbol{E}_{te}^{\phi} + \frac{1}{\rho}\boldsymbol{E}_{te}^{\phi} : \frac{\partial \mathbb{C}^{\phi}}{\partial T} : \boldsymbol{\alpha}^{\phi}\left(T - T_0\right) \\ & + \frac{1}{\rho}\boldsymbol{E}_{te}^{\phi} : \mathbb{C}^{\phi} : \boldsymbol{\alpha}^{\phi} - \frac{1}{2\rho}\boldsymbol{\alpha}^{\phi} : \left(\frac{\partial \mathbb{C}^{\phi}}{\partial T} - \frac{\partial \tilde{\mathbb{C}}^{\phi}}{\partial T}\right) : \boldsymbol{\alpha}^{\phi}\left(T - T_0\right)^2 \\ & - \frac{1}{\rho}\boldsymbol{\alpha}^{\phi} : \left(\mathbb{C}^{\phi} - \tilde{\mathbb{C}}^{\phi}\right) : \boldsymbol{\alpha}^{\phi}\left(T - T_0\right) \\ & + \tilde{c}^{\phi}\ln\left[\frac{T}{T_0}\right] - \frac{1}{2\rho}\frac{\partial H^{\phi}}{\partial T}(1-D)\sum_{s}\lambda_s^{\phi}\sum_{t}h_{st}^{\phi}\lambda_t \end{aligned} \tag{27}$$

The thermodynamic force associated with the hardening variable λ_s^{ϕ} is denoted by r_s^{ϕ}. The corresponding state equation is:

$$r_s^{\phi} = \rho\frac{\partial a^{\phi}}{\partial \lambda_s^{\phi}} = H^{\phi}(1-D)\sum_{t}h_{st}^{\phi}\lambda_t^{\phi} \tag{28}$$

In the following, the variable r_s^{ϕ} is referred to as the Critical Resolved Shear Stress (CRSS) of the sth slip system. It measures the resistance to plastic deformation of a given slip system. The energy restitution rate Y^{ϕ}, which is the driving force for the development of damage, is given by:

$$Y^{\phi} = -\rho\frac{\partial a^{\phi}}{\partial D} = \frac{1}{2}H^{\phi}\sum_{s}\lambda_s^{\phi}\sum_{t}h_{st}^{\phi}\lambda_t^{\phi} - \frac{1}{2\rho}\boldsymbol{E}_{e}^{\phi} : \frac{\partial \mathbb{C}^{\phi}}{\partial D} : \boldsymbol{E}_{e}^{\phi} \tag{29}$$

It is worth mentioning that, though the damage variable is the same for all variants, the energy restitution rate Y^{ϕ} is different. Also, the

derivative of the stiffness tensor $\mathbb{C}^\phi$ with respect to the damage variable is given by:

$$\frac{\partial \mathbb{C}^\phi}{\partial D} = \begin{cases} -\tilde{\mathbb{C}}^\phi, & \text{tr}[\boldsymbol{E}_e^\phi] > 0 \\ -\tilde{\mathbb{C}}^\phi + \mathbb{P}_s : \tilde{\mathbb{C}}^\phi : \mathbb{P}_s, & \text{tr}[\boldsymbol{E}_e^\phi] \leq 0 \end{cases} \tag{30}$$

The damage variable is therefore representative of the degradation of the mechanical properties of a material point, rather than that of a specific variant. In contrast with physically-based models that explicitly consider the impact nucleation, growth and coalescence of cavities (Ling et al. (2016),Scherer et al. (2021)), the present approach is purely phenomenological and does not consider damage-induced anisotropy.

2.3. Evolution equations

Dissipation source. In the absence of heat conduction, the specific dissipation source d^ϕ for variant ϕ is given by:

$$d^\phi = p^\phi - \dot{a}^\phi - s^\phi \dot{T} \tag{31}$$

Combining the expression of the specific power developed by internal forces (13) with the state Eqs. (26), (27), (28) and (29) allows re-writing the specific dissipation source as follows:

$$d^\phi = \frac{1}{\rho}\boldsymbol{\Sigma}^\phi : \boldsymbol{L}_p^\phi - \frac{1}{\rho}\sum_s r_s^\phi \dot{\lambda}_s^\phi + \frac{1}{\rho} Y^\phi \dot{D} \tag{32}$$

According to the above equation, heat dissipation is the consequence of the accumulation of plastic deformation and/or the development of damage. Also, this equation indicates that the plastic work is not entirely dissipated into heat because of the contribution of hardening to energy storage. Introducing the resolved shear stress $\tau_s^\phi = \boldsymbol{m}_s^\phi \cdot \boldsymbol{\Sigma}^\phi \cdot \boldsymbol{n}_s^\phi$ leads to the following expression of the specific dissipation source:

$$d^\phi = \frac{1}{\rho}\sum_s \left(\tau_s^\phi \dot{\gamma}_s - r_s^\phi \dot{\lambda}_s^\phi\right) + \frac{1}{\rho} Y^\phi \dot{D} \tag{33}$$

According to Eq. (11), the specific dissipation source d for a material point is obtained from the addition of the contributions of the different variants, that is:

$$d = \sum_\phi \left(\frac{1}{\rho}\sum_s \left(\tau_s^\phi \dot{\gamma}_s^\phi - r_s^\phi \dot{\lambda}_s^\phi\right)\right) + \frac{1}{\rho} Y \dot{D} \tag{34}$$

where the energy restitution rate Y is defined from:

$$Y = \sum_\phi \zeta^\phi Y^\phi \tag{35}$$

The above equation indicates that the flux variables $\dot{\gamma}_s^\phi$, $\dot{\lambda}_s^\phi$ and $\dot{D}$ are connected to the dissipative forces τ_s^ϕ, r_s^ϕ and Y.

Viscoplastic flow rule. In the context of rate-dependent plasticity, it is possible to construct the flow rule from Orowan's equation. Indeed, according to Orowan's equation, the plastic shear strain rate for each slip system is connected to the average dislocation velocity v_s^ϕ and the mobile dislocation density $\varrho_{m,s}^\phi$ according to:

$$\dot{\gamma}_s^\phi = \varrho_{m,s}^\phi b_s^\phi v_s^\phi \tag{36}$$

In the present work, the mobile dislocation density is assumed to be equal to some fraction β of the total dislocation density so that:

$$\varrho_{m,s}^\phi = \beta \varrho_s^\phi = \beta \left(\frac{\lambda_s^\phi}{b_s^\phi}\right)^2 \tag{37}$$

Also, for the estimation of the average dislocation velocity, a simple power law is used:

$$v_s^\phi = v_0^\phi \left\langle \frac{\left|\tau_s^\phi\right| - r_s^\phi}{K_s^\phi} \right\rangle^{n_s^\phi} \tag{38}$$

where n_s^ϕ and K_s^ϕ are some temperature-dependent viscosity parameters and v_0^ϕ is a reference dislocation velocity. The viscoplastic rule is obtained by combining Eqs. (36), (37) and (38), which leads to:

$$\dot{\gamma}_s^\phi = \beta \frac{(\lambda_s^\phi)^2}{b_s^\phi} v_0^\phi \left\langle \frac{\left|\tau_s^\phi\right| - r_s^\phi}{K_s^\phi} \right\rangle^{n_s^\phi} \tag{39}$$

$$= \left(\lambda_s^\phi\right)^2 \left\langle \frac{\left|\tau_s^\phi\right| - r_s^\phi}{k_s^\phi} \right\rangle^{n_s^\phi} \tag{40}$$

In the above equation, k_s^ϕ is a temperature-dependent material parameter that needs to be defined for each slip system. The description of hardening assumes that the evolution of the dislocation density is controlled by the competition between dislocation multiplication and dislocation annihilation. Adopting the proposition of Mecking and Kocks (1981), the evolution equation for the dislocation density is:

$$\dot{\varrho}_s^\phi = \left(\kappa_m^\phi \sqrt{\varrho_s^\phi} - \kappa_a^\phi \varrho_s^\phi\right) |\dot{\gamma}_s^\phi| \tag{41}$$

where κ_m^ϕ (respectively κ_a^ϕ) is a material parameter that controls dislocation multiplication (respectively dislocation annihilation). Using the definition (19) of the isotropic hardening variable, one obtains the corresponding evolution equation:

$$\dot{\lambda}_s^\phi = \left(1 - B_s^\phi \lambda_s^\phi\right) |\dot{\gamma}_s^\phi| \tag{42}$$

with:

$$\kappa_m^\phi = \frac{2}{b_s^\phi} \text{ and } \kappa_a^\phi = 2B_s^\phi \tag{43}$$

It should be mentioned that the material parameter B_s^ϕ, which controls the asymptotic value of the hardening variable, is assumed to depend on temperature.

Damage rule. For the evolution of the damage variable, a power-law is used:

$$\dot{D} = \left\langle \frac{Y - Y_r}{S} \right\rangle^m (1 - D) \tag{44}$$

In the above equation, S, m and Y_r are material parameters controlling the rate of damage accumulation. Specifically, Y_r is a threshold that defines the minimum energy restitution rate for the development of damage. Also, the factor $(1 - D)$ is introduced to prevent the damage variable from exceeding unity.

2.4. Heat sources

To model the thermo-mechanical behavior of the Ti17 alloy, the heat diffusion equation must be established. For the construction of the heat diffusion equation, it is convenient to introduce the following quantities. First, for a variant ϕ, the thermoelastic source φ_{te}^ϕ is obtained from:

$$\varphi_{te}^\phi = -T \frac{\partial s^\phi}{\partial \boldsymbol{E}_{te}^\phi} : \dot{\boldsymbol{E}}_{te}^\phi \tag{45}$$

Also, the internal coupling source φ_{ic}^ϕ associated with the ϕth variant is expressed as follows:

$$\varphi_{ic}^\phi = -T \sum_s \frac{\partial s^\phi}{\partial \lambda_s^\phi} \dot{\lambda}_s^\phi - T \frac{\partial s^\phi}{\partial D} \dot{D} \tag{46}$$

Finally, the specific heat capacity c^ϕ is given by:

$$c^\phi = T \frac{\partial s^\phi}{\partial T} \tag{47}$$

It is worth mentioning that, because of the impact of temperature on stiffness and hardening properties, the specific heat capacity c^ϕ of a given variant is not constant during a deformation process.

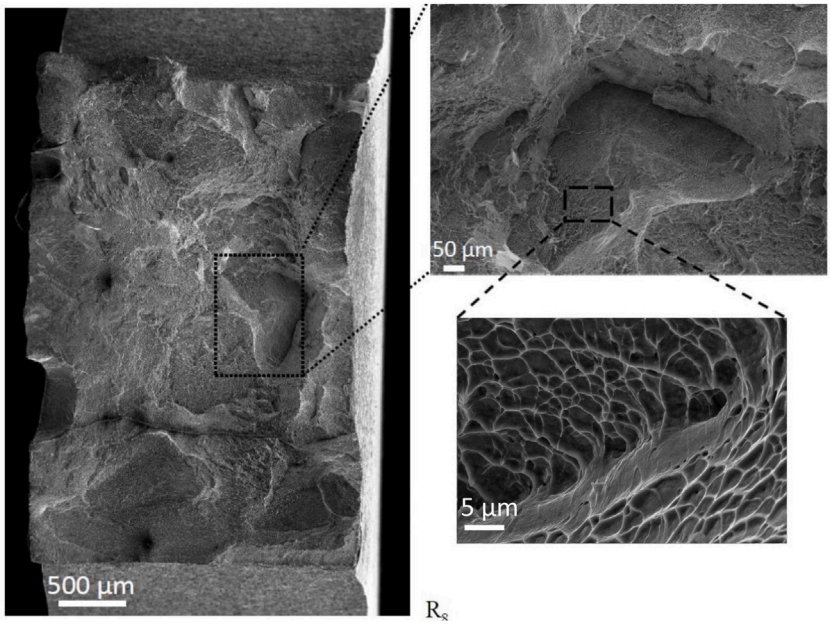

Fig. 3. SEM observations of the as-received $\alpha+\beta$ Ti17 titanium alloy deformed at a strain rate of 0.1 s^{-1}, a temperature of 25 °C showing the ductile aspect of fracture.

From the state Eq. (27), one obtains the following expression of specific dissipation source:

$$\dot{d}^{\phi} = \dot{s}^{\phi} T \tag{48}$$

$$= T\frac{\partial s^{\phi}}{\partial T}\dot{T} + T\frac{\partial s^{\phi}}{\partial \boldsymbol{E}_{te}^{\phi}} : \dot{\boldsymbol{E}}_{te}^{\phi} + T\sum_{s}\frac{\partial s^{\phi}}{\partial \lambda_{s}^{\phi}}\dot{\lambda}_{s}^{\phi} + T\frac{\partial s^{\phi}}{\partial D}\dot{D} \tag{49}$$

Using the definitions (45), (46) and (47), the above equation is re-arranged as follows:

$$c^{\phi}\dot{T} = d^{\phi} + \varphi_{ic}^{\phi} + \varphi_{te}^{\phi} \tag{50}$$

It is worth mentioning that, because of the impact of temperature on stiffness and hardening properties, the specific heat capacity c^{ϕ} of a given variant is not constant during a deformation process. The specific heat capacity c^{ϕ} is equal to the initial specific heat capacity $\tilde{c}^{\phi}$ when (i) the current temperature is equal to the reference temperature T_0, (ii) the thermoelastic strain tensor is zero and (iii) the hardening variables associated with the different slip systems vanish. The heat diffusion equation for a material point is obtained by summing the contributions of the different constituents:

$$c\dot{T} = d + \varphi_{ic} + \varphi_{te} \tag{51}$$

with:

$$c = \sum_{\phi}\zeta^{\phi}c^{\phi} \tag{52}$$

$$\varphi_{te} = \sum_{\phi}\zeta^{\phi}\varphi_{te}^{\phi} \tag{53}$$

$$\varphi_{ic} = \sum_{\phi}\zeta^{\phi}\varphi_{ic}^{\phi} \tag{54}$$

3. Parameter identification

3.1. Summary of experimental results

To investigate both the flow behavior and the damage behavior of the present Ti17 alloy, different experimental tests have been carried out. The experimental procedure used for such tests is briefly described here. A detailed description of the experimental setup can be found in Ben-Boubaker et al. (2020).

First, some uniaxial compression tests have been conducted on a fully β microstructure at different temperatures (from 25 °C to 900 °C) and different strain rates (from 0.1 s^{-1} to 10 s^{-1}). For these tests, cylindrical specimens (with a diameter of 6 mm and a height of 9 mm) have been used. To obtain a fully β-microstructure, these specimens have been heat treated at 950 °C for 30 min, then rapidly cooled to the test temperature and deformed under uniaxial compression. The corresponding stress–strain curves are plotted in Fig. 7.

Second, some uniaxial compression tests have also been performed on cylindrical specimens with the as-received $\alpha+\beta$ microstructure presented in Fig. 1. To avoid phase transformation, these specimens have been heated from room temperature to the test temperature (from 25 °C to 800 °C) with a rate of 100 °C/s. Once the test temperature was reached, the specimen has been deformed with a constant nominal axial strain rate (from 0.1 s^{-1} to 10 s^{-1}). The results of these tests are shown in Fig. 8.

Third, to characterize the impact of loading conditions (i.e. temperature, strain rate and triaxiality) on ductile damage, some tension tests have been carried out on some flat specimens with the as-received $\alpha+\beta$ microstructure. As illustrated by Fig. 4, some smooth and notched specimens have been used for these tests. Depending on the notch geometry, the triaxiality ratio changes from zero (pure shear) to 0.72 (close to biaxial tension). These specimens have been deformed at various strain rates and various temperatures until fracture was detected. The results of these tests are presented in Fig. 9. For the purpose of illustration, a typical fracture surface showing the ductile aspect of fracture is shown in Fig. 3. This feature of fracture surfaces is observed whatever the loading conditions (temperature and strain rate) are.

3.2. Material parameters

3.2.1. Numerical models

To identify the material parameters of the proposed model for the Ti17 alloy, an inverse method has been used. First, the results of the uniaxial compression tests have been used to adjust the parameters of the viscoplastic flow rule and the isotropic hardening rule. For the application of the inverse method, the proposed constitutive model has been implemented within the ABAQUS Explicit finite element solver. The numerical model used to simulate uniaxial compression tests is presented in Fig. 5. The corresponding microstructure, which has been generated with the NEPER software (Quey et al., 2011), contains approximately 1200 grains. The average number of elements per grain

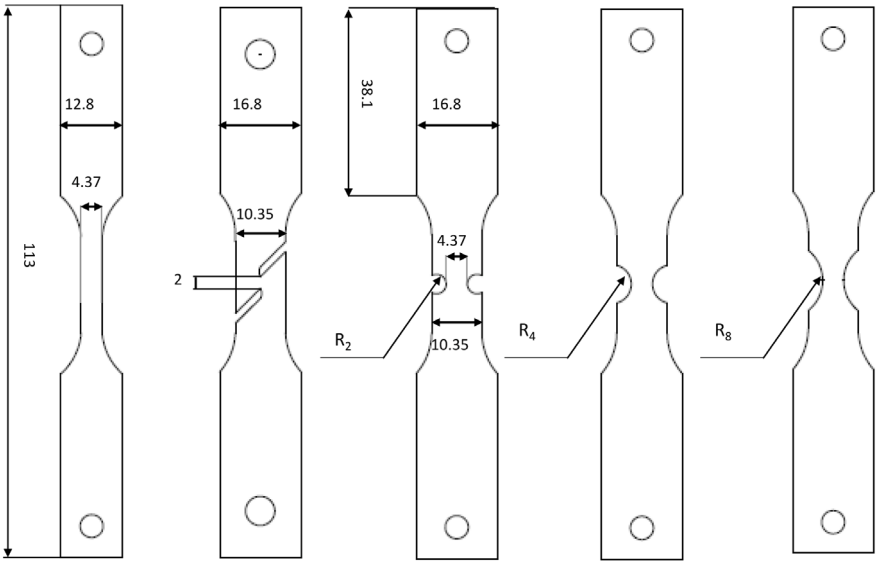

Fig. 4. Geometries of smooth and notched specimens.

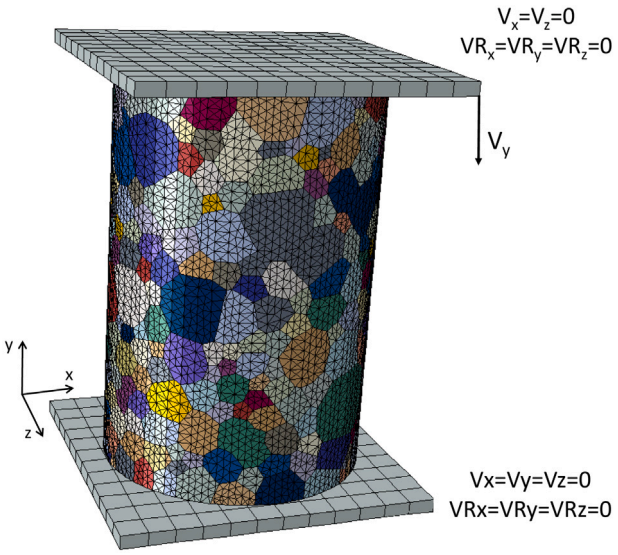

Fig. 5. Geometrical model and boundary conditions for the simulation of compression tests.

is about 170, which is sufficient to achieve convergence. To account for friction at the interface between the specimen and the anvils, a Coulomb model with a friction coefficient of 0.3 is used (Li et al., 2001).

Second, the tension test results have been used to estimate the parameters of the damage model. The numerical models presented in Fig. 6 are used for the simulation of tension tests. These models, which only consider the gauge volume of tension specimens, have first been generated with the NEPER software (Quey et al., 2011). Then, the notches have been introduced by removing elements and adjusting node positions in the vicinity of the notch. The numerical model contains approximately 500 grains. For the simulation of tension tests, the real grain size of 800 μm is used. Each grain is meshed with C3D4 tetrahedral elements, with an average number of 500 elements per grain. As mentioned earlier, in the context of adiabaticity, heat exchanges are neglected when performing numerical simulations of compression and tension tests.

Table 2
Material parameters for the β phase. The Kelvin scale is used for temperature.

Parameters	Values
k_s^β (MPa)	$157-0.12\ T$
n^β	$25\ \exp(-0.001\ T)$
H^β (MPa)	$1320\ \exp(-0.0032\ T)$
B_s^β	$4\ \exp(0.03\ T)$

3.2.2. Viscoplastic and hardening parameters of the β phase

To model the viscoplastic behavior of the β phase, crystallographic slip is assumed to occur on the $\langle 111\rangle\{110\}$ and $\langle 111\rangle\{112\}$ slip systems (Orlans-Joliet et al., 1988; Liang and Khan, 1999; Lewis et al., 2010; Lhadi et al., 2018). The material parameters for the β phase are listed in Table 2. An initial dislocation density of 4×10^{15} m^{-2} is assumed for all slip systems. Following the suggestion of Martin et al. (2014), no distinction is made between self- and latent hardening. As a result, the coefficients of the interaction matrix h are all equal to unity. Also, some parameters, including the elastic constants (Martin et al., 2014), the thermal expansion coefficient (Liang and Khan, 1999) and the initial specific heat Teixeira et al. (2006), have been extracted from literature. The remaining viscoplastic and hardening parameters of the β phase have been adjusted as a function of temperature to reproduce the experimental nominal stress *versus* nominal strain curves obtained for the β-treated microstructure. For this purpose, each grain of the numerical model is composed of a single β phase variant, which has been assigned a random crystallographic orientation. As illustrated by Fig. 7, the flow behavior of the β-treated microstructure is generally well described by the numerical model. For low temperatures ($T \leq 450$ °C), the maximum error between the experimental and numerical curves does not exceed 6%. For temperatures above 700 °C, a yield drop phenomenon, which is attributed to either dynamic recrystallization Ben-Boubaker et al. (2020) or the multiplication of mobile dislocations Teixeira et al. (2007), is observed. This phenomenon is partly captured by the proposed model. Specifically, while the contribution of dynamic recrystallization is ignored, the role of mobile dislocations on the development of plasticity is explicitly accounted in the flow rule as (see Eqs. (37)–(40)).

3.2.3. Viscoplastic and hardening parameters of the α phase

The description of the viscoplastic behavior of the α phase assumes that crystallographic slip is restricted to the basal $\langle 11\bar{2}0\rangle\{0001\}$, prismatic $\langle 11\bar{2}0\rangle\{10\bar{1}0\}$, pyramidal $\langle a\rangle$ $\langle 11\bar{2}0\rangle\{1\bar{1}01\}$ and pyramidal $\langle c+a\rangle$

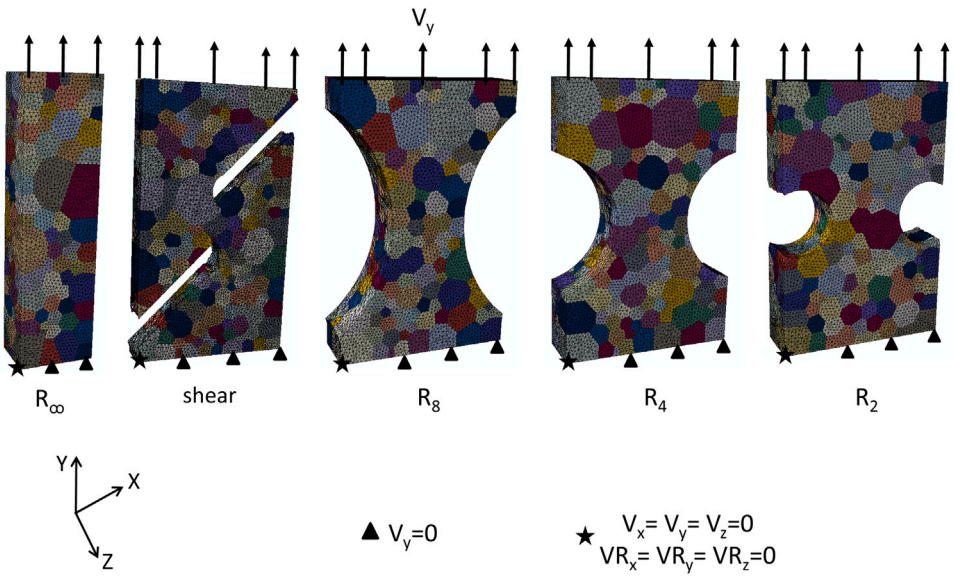

Fig. 6. Geometrical model and boundary conditions for the simulation of tension tests.

Table 3
Material parameters for the α phase. The Kelvin scale is used for temperature.

Parameters	Values
k_s^α (MPa)	$539-0.4\ T$
n^α	$172\ \exp(-0.002\ T)$
H^α (MPa)	$1970\ \exp(-0.0042\ T)$
B_s^α	$9\ \exp(0.002\ T)$

$\langle 11\bar{2}3\rangle\{\bar{1}011\}$ slip systems (Zhang et al., 2016; Kasemer et al., 2017). The same value as for the β-phase is used for the initial dislocation density for all slip systems. The material parameters of the α phase are presented in Table 3. The elastic constants (Martin et al., 2014), the thermal expansion coefficients (Martin et al., 2014) and initial specific heat Teixeira et al. (2006) have been extracted from literature. The material parameters involved in the viscoplastic flow rule and the hardening rule have been selected to reproduce the results of uniaxial compression tests obtained for the as-received $\alpha+\beta$ microstructure. To perform the corresponding simulations, each grain is composed of a single β phase variant with a random crystallographic orientation and multiple α phase variants. Based on the experimental observations conducted by Salib et al. (2013), no α phase variant selection phenomenon is considered. As a result, the α phase variants contained within an element are randomly selected amongst the twelve possible variants obtained from the Burgers orientation relationship:

$$\{110\}_\beta \| (0001)_\alpha \text{ and } \langle 111\rangle_\beta \| \left[11\bar{2}0\right]_\alpha \tag{55}$$

The numerical nominal stress *versus* nominal strain curves obtained after parameter identification are plotted in Fig. 8. The agreement with experimental results is correct. Specifically, the decrease of the hardening rate with an increasing temperature is correctly depicted.

3.2.4. Damage parameters for the as-received $\alpha+\beta$ Ti17 microstructure

The damage parameters have been adjusted to reproduce the nominal stress–strain curves obtained from tension tests. As for uniaxial compression specimens, each grain consists of a single β phase variant with a random crystallographic orientation and multiple α phase variants. The resulting damage parameters are listed in . As illustrated by Fig. 9, the beneficial effect of an increasing temperature and/or a decreasing strain rate on ductility is correctly captured by the numerical model.

Parameters	Values
Y_r (MPa)	$49\ \exp(-0.0014\ T(\mathrm{K}))$
S (MPa)	5
m	6.2

4. Discussion

4.1. Impact of temperature on strain localization

The experimental results obtained for compression tests (Ben-Boubaker et al., 2020) indicate that the deformation behavior is impacted by strain localization. Specifically, as illustrated by Figs. 10 and 11, two strain localization modes have been observed. The first mode, which is observed at high temperatures, leads to the formation of a Highly Deformed Region (HDR) in the center of the specimen. The second strain localization mode, which is predominant at low temperatures, results from the formation of an Adiabatic Shear Band (ASB).

The numerical results for a compression specimen deformed with a strain rate of 10 s^{-1} and an initial temperature of 25 °C are shown in Fig. 10. The numerical results are consistent with experimental observations. Indeed, a shear band, with an angle of approximately ±45° with respect to the compression direction, is clearly detected at the end of the compression test. As shown in Fig. 10, the crack initiates at the two tips of the band and then propagates along the shear direction. The formation of the shear band is mostly explained by the local temperature elevation, which reaches 160 °C at the instant of fracture.

For an initial temperature of 800 °C (see Fig. 11), the temperature elevation is much lower (about 120 °C) and less localized. Since the maximum temperature is obtained within the central region of the specimen, plastic deformation tends to concentrates in this region. The resulting highly deformed region is oriented perpendicular to the compression direction, which is consistent with experimental results.

4.2. Impact of local microstructure on ductile fracture

To evaluate the sensitivity of the proposed damage model to the local microstructure, some simulations have been performed using four different sets of crystallographic orientations for smooth and notched specimens. For the different sets of orientations, the crystallographic texture is globally the same (i.e. random) but locally different. The initial temperature is set to 25 °C while the nominal strain rate is fixed to 1 s^{-1} for all simulations.

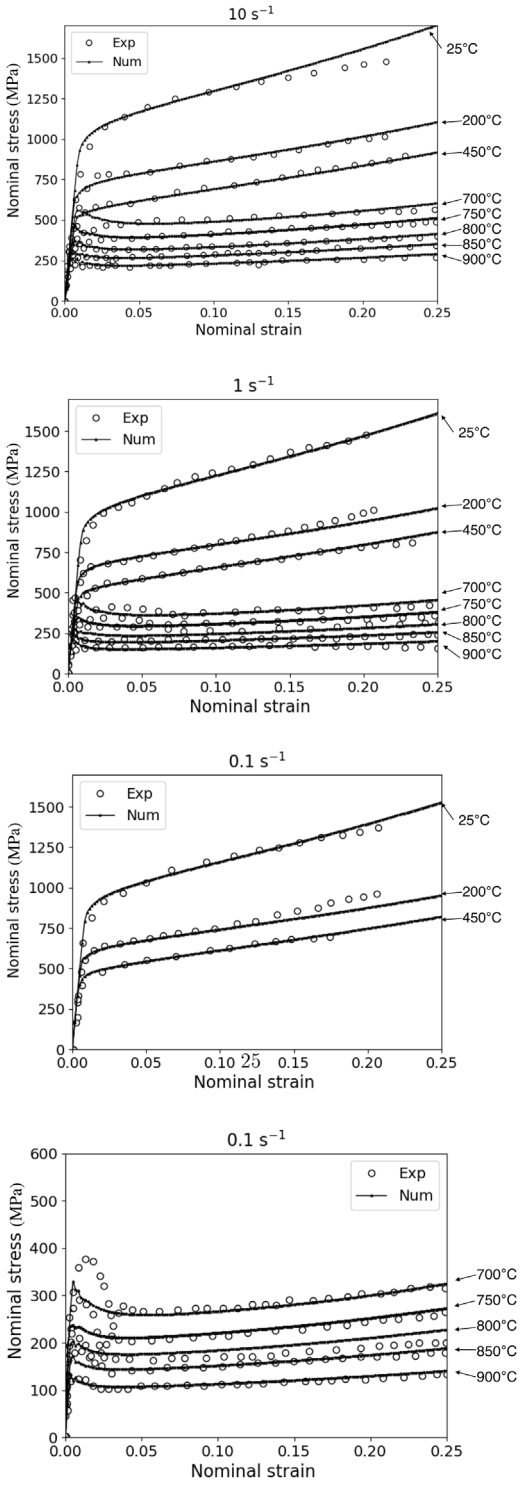

Fig. 7. Comparison between the numerical and experimental nominal stress–nominal strain curves obtained under uniaxial compression for the β-treated Ti17 microstructure.

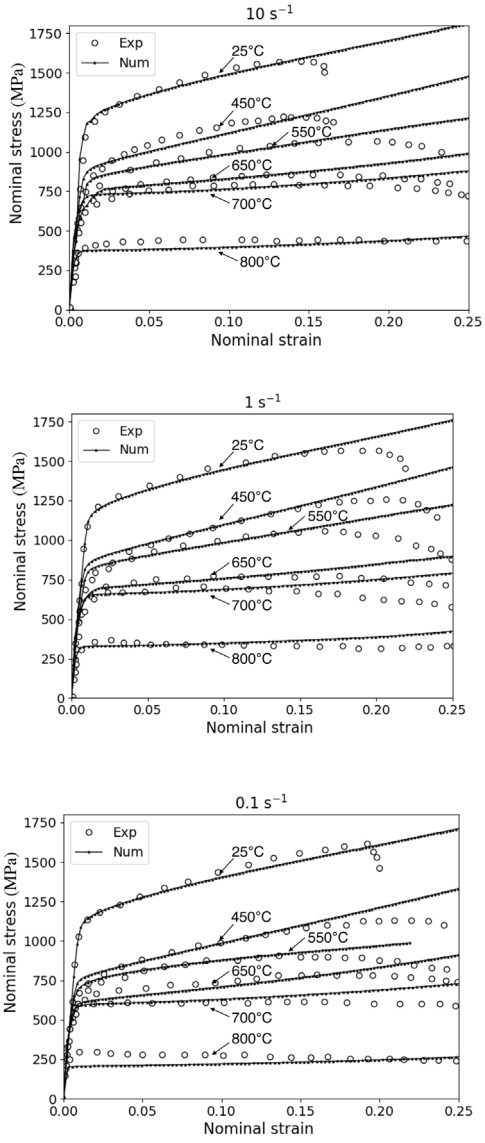

Fig. 8. Comparison between the numerical and experimental nominal stress–nominal strain curves obtained under uniaxial compression for the as-received $\alpha + \beta$ Ti17 microstructure.

The nominal stress–strain curves obtained for the different specimen geometries are plotted in Fig. 12. For both smooth and notched specimens, the flow behavior is not much affected by the local microstructure. However, when looking at the fracture strain, some discrepancies between the specimen geometries are observed. For smooth tension specimens, the impact of the local microstructure on the fracture strain is limited. At the opposite, for notched specimens, especially shear specimens, the fracture strain changes quite importantly for the different orientation sets. This sensitivity to the local microstructure is largely explained by the gauge volume, which varies significantly between smooth and notched specimens. Indeed, as shown in Fig. 13, damage is constrained to develop within the few grains placed between notches for notched specimens. The progression of ductile damage is therefore largely dependent on the crystallographic orientation of these few grains. At the opposite, for smooth specimens, the development of ductile damage is not constrained by the specimen geometry. The number of grains possibly affected by damage is much higher than for notched specimens, which explains why the crack initiation site changes for the different orientation sets.

The above results indicate that care should be taken when investigating the damage behavior of coarse-grained materials. Indeed, the results obtained for notched specimens are possibly not representative of the global behavior.

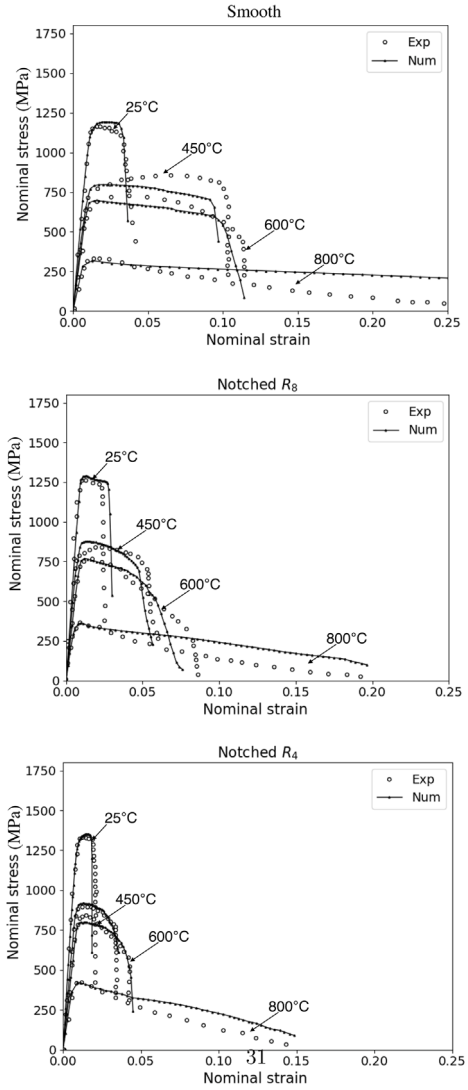

Fig. 9. Comparison between the numerical and experimental nominal stress–nominal strain curves obtained under tension for the as-received $\alpha + \beta$ Ti17 microstructure for smooth and notched specimens.

4.3. Impact of crystallographic texture on ductile fracture

To investigate the impact of texture on the development of ductile damage, some uniaxial tension tests, with different crystallographic textures for the β phase, have been simulated. Specifically, different sets of orientations, with either the <100>, <110> or <111> directions aligned with the loading direction, have been generated for the β phase. For the α phase, no specific variant selection procedure has been used.

The nominal stress–strain curves obtained for the different fiber textures for an initial temperature of 25 °C and a nominal strain rate of 1 s^{-1} are plotted in Fig. 14. The flow behavior is not much affected by the crystallographic texture of the β phase. The effect of the crystallographic texture of the β phase on the flow behavior is limited mostly for two reasons. First, the development of plasticity is also controlled by the α phase, which is predominant for the Ti17 alloy. Second, because many slip systems can be activated, the plastic deformation anisotropy of the β phase is not very important.

In contrast with the flow behavior, the development of ductile damage in smooth specimens is dependent on the crystallographic texture. Specifically, the fracture strain is minimal for <111> fiber texture and maximum for <100> fiber texture.

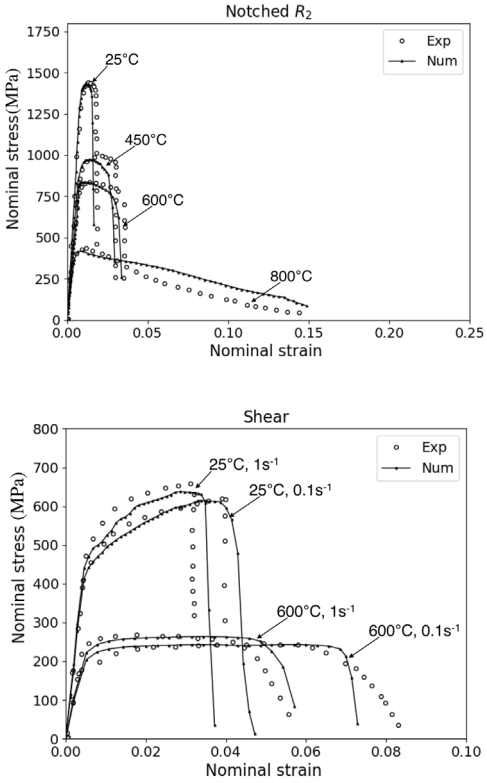

Fig. 9. (*continued*).

4.4. Impact of heat exchanges

To evaluate the impact of heat exchanges, the cases of adiabatic and isothermal uniaxial tension are examined. For this purpose, a nominal strain rate of 1 s^{-1} is imposed to the smooth tension specimen. Two different initial temperatures, of either 25 °C or 800 °C, are considered. The nominal stress–strain curves obtained for the different conditions are plotted in Fig. 15. For both temperatures, the flow stress obtained under adiabatic conditions is inferior to that obtained for isothermal conditions as a result of thermal softening. However, while the impact of heat exchanges is limited at 800 °C, their role on the deformation behavior cannot be ignored at 25 °C.

The above results suggest that particular care should be taken when investigating the impact of strain rate on the deformation behavior. While isothermal conditions are representative of low strain rates, adiabatic conditions are appropriate for high strain rates. As a result, from an experimental perspective, the strain rate effect cannot be fully decoupled from that of temperature, especially for low temperatures and high strain rates (Zaera et al., 2013; Jovic et al., 2006).

5. Conclusion

In this work, a crystal plasticity-based constitutive model has been proposed to describe the behavior of the $\alpha + \beta$ Ti17 alloy under extreme loading conditions. The constitutive relations are developed in the context of finite strains using the general framework of crystal plasticity. To consider ductile fracture, a damage variable is introduced to describe the progressive stiffness reduction when the material is subjected to severe loading conditions. The constitutive relations have been implemented in the ABAQUS/Explicit finite element solver with a user-defined subroutine. The model parameters have been identified for the Ti17 alloy using the experimental results obtained for tension and compression tests. According to the results, the numerical and

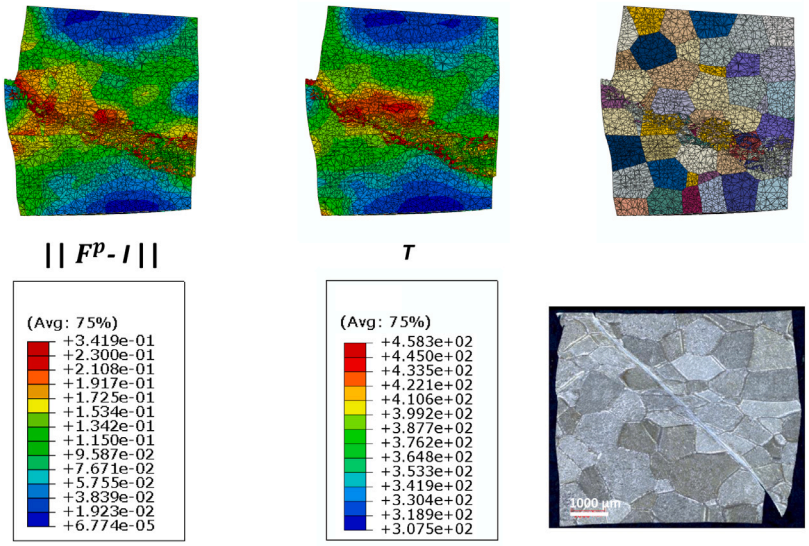

Fig. 10. Evaluation of instantaneous local variables (equivalent plastic contribution to the deformation gradient field $\|\boldsymbol{F}^p - \boldsymbol{I}\|$ and temperature field T) at the instant of failure for $\alpha + \beta$ Ti17 specimen deformed in compression at 10 s^{-1} and 25 °C.

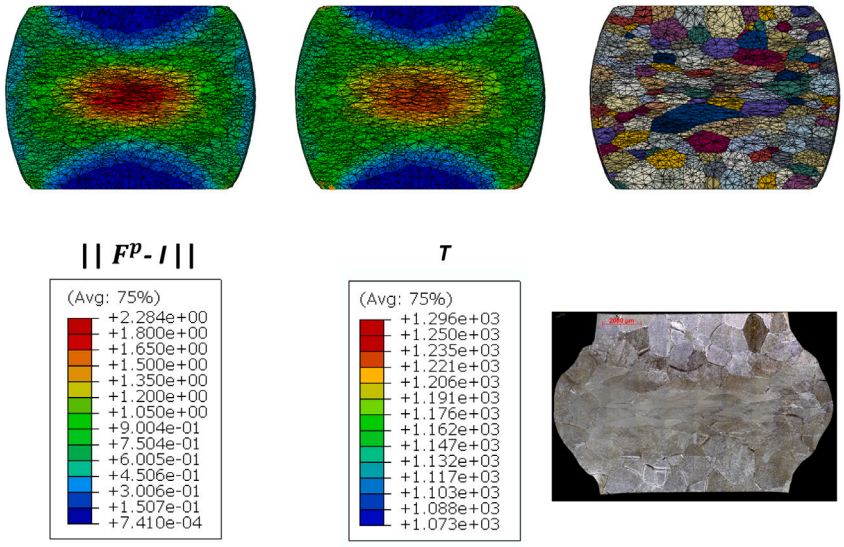

Fig. 11. Evaluation of instantaneous local variables (equivalent plastic contribution to the deformation gradient field $\|\boldsymbol{F}^p - \boldsymbol{I}\|$ and temperature field T) at an axial strain of 30% for an $\alpha + \beta$ Ti17 specimen deformed in compression at 10 s^{-1} and 800 °C.

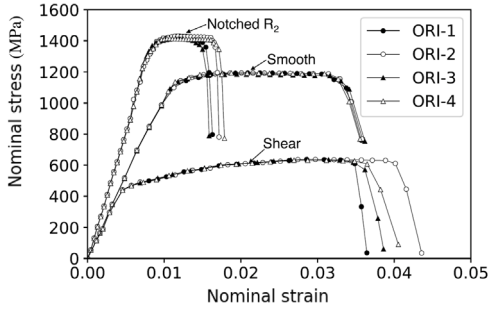

Fig. 12. Impact of local microstructure on the numerical nominal stress–nominal strain curves obtained under different tension tests. The temperature and the strain rate are set to 25 °C and 1 s^{-1}, respectively.

experimental nominal stress–strain curves of the different tests are in good agreement.

The proposed model provides a consistent description of the impact of temperature on strain localization. Specifically, the different strain localization modes observed under uniaxial compression depending on the temperature are correctly reproduced. Also, the numerical results obtained for notched specimens indicate that, because of the coarse-grained microstructure, the fracture strain is highly dependent on the local microstructure, which does not guarantee representativity. Finally, the impact of heat exchanges on the deformation behavior cannot be ignored for low temperatures.

Further work will focus on the application of the proposed model to the specific context of machining. Specifically, the model will be used to investigate the impact of microstructure and processing conditions on the chip morphology and cutting forces for the Ti17 alloy. Also, at this stage, no regularization technique is used to limit mesh dependency.

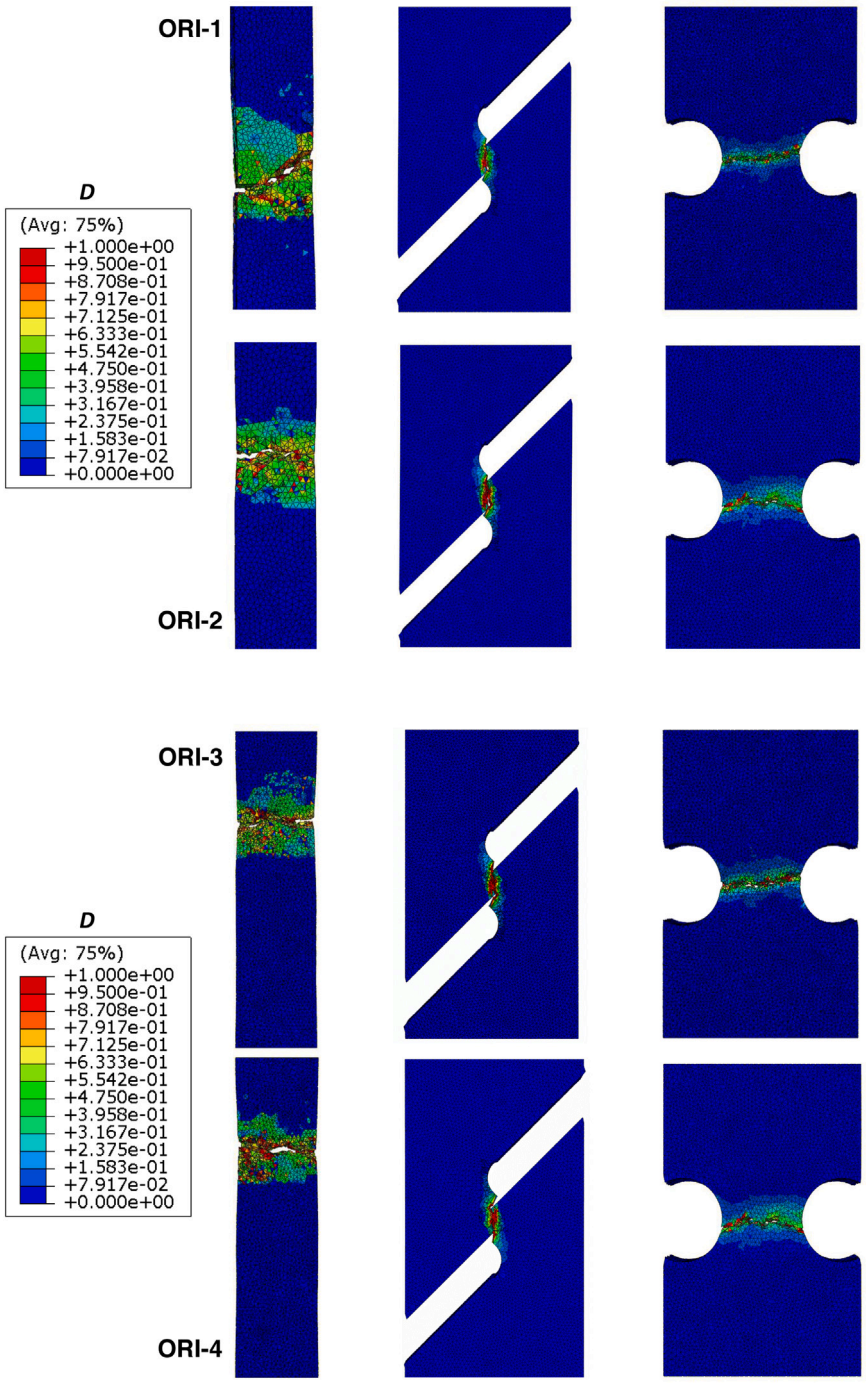

Fig. 13. Impact of the local microstructure on the damage field D for smooth and notched specimens deformed at a temperature of 25 °C and a strain rate of 1 s^{-1}.

While the current approach allows describing the initial stage of ductile failure, the description of the final stage leading to total failure is possibly mesh-dependent. As suggested by Scherer et al. (2021), crystal plasticity-based gradient models can be adopted in the context of ductile damage to circumvent such difficulties.

CRediT authorship contribution statement

H.B. Boubaker: Software, Analysis, Investigation, Resources, Data curation, Writing – original draft, Visualization. **C. Mareau:** Software, Validation, Methodology, Review and editing, Supervision. **Y. Ayed:** Validation, Methodology, Review and editing, Supervision. **G. Germain:** Review, Supervision, Project administration, Funding acquisition. **A. Tidu:** Review, Supervision.

Declaration of competing interest

The authors declare that they have no known competing financial interests or personal relationships that could have appeared to influence the work reported in this paper.

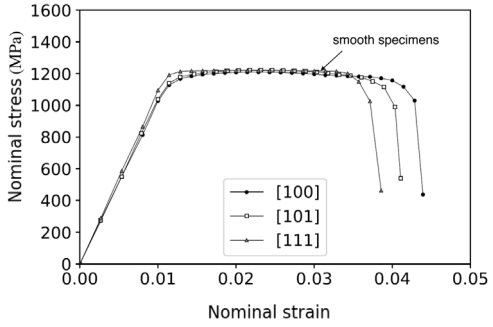

Fig. 14. Impact of the β-grains orientation on the numerical nominal stress–nominal strain curves obtained under tension for $\alpha + \beta$ Ti17 smooth specimens deformed at a temperature of 25 °C and a strain rate of 1 s^{-1}.

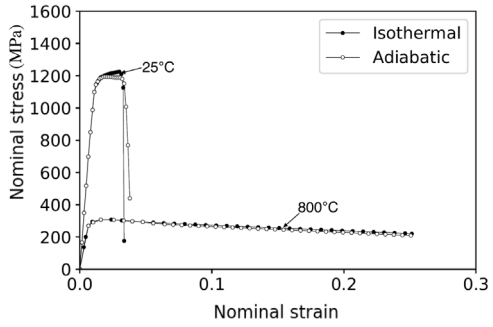

Fig. 15. Impact of heat exchanges on the numerical nominal stress–nominal strain curves obtained under tension for $\alpha + \beta$ Ti17 specimens deformed at a strain rate of 1 s^{-1} and two temperatures: 25 °C and 800 °C.

Acknowledgments

This research was supported by two French organizations from "Angers Loire Metropole": "Angers Loire Development" and "Angers Technopole." The authors would like to acknowledge their financial support.

References

Abdolvand, H., Louca, K., Mareau, C., Majkut, M., Wright, J., 2020. On the nucleation of deformation twins at the early stages of plasticity. Acta Mater. 196, 733–746. http://dx.doi.org/10.1016/j.actamat.2020.07.010, URL http://www.sciencedirect.com/science/article/pii/S1359645420305085.

Abukhshim, N., Mativenga, P., Sheikh, M., 2006. Heat generation and temperature prediction in metal cutting: A review and implications for high speed machining. Int. J. Mach. Tools Manuf. 46 (7), 782–800. http://dx.doi.org/10.1016/j.ijmachtools.2005.07.024, URL http://www.sciencedirect.com/science/article/pii/S089069550500180X.

Arrazola, P., Garay, A., Iriarte, L., Armendia, M., Marya, S., tre, F.L.M., 2009. Machinability of titanium alloys (Ti6Al4V and Ti5553). J. Mater. Process. Technol. 209 (5), 2223–2230. http://dx.doi.org/10.1016/j.jmatprotec.2008.06.020, URL http://www.sciencedirect.com/science/article/pii/S0924013608004998.

Asaro, R., 1983. Micromechanics of crystals and polycrystals. Adv. Appl. Math. Mech. 23 (1), 115.

Aslan, O., Quilici, S., Forest, S., 2011. Numerical modeling of fatigue crack growth in single crystals based on microdamage theory. Int. J. Damage Mech. 20 (5), 681–705. http://dx.doi.org/10.1177/1056789510395738.

Ayed, Y., Robert, C., Germain, G., Ammar, A., 2016. Development of a numerical model for the understanding of the chip formation in high-pressure water-jet assisted machining. Finite Elem. Anal. Des. 108, 1–8. http://dx.doi.org/10.1016/j.finel.2015.09.003, URL http://www.sciencedirect.com/science/article/pii/S0168874X15001389.

Bache, M.R., Dunne, F.P.E., Madrigal, C., 2010. Experimental and crystal plasticity studies of deformation and crack nucleation in a titanium alloy. J. Strain Anal. Eng. Des. 45 (5), 391–399. http://dx.doi.org/10.1243/03093247JSA594.

Baker, M., 2006. Finite element simulation of high-speed cutting forces. J. Mater. Process. Technol. 176 (1), 117–126. http://dx.doi.org/10.1016/j.jmatprotec.2006.02.019, URL http://www.sciencedirect.com/science/article/pii/S0924013606002020.

Bammann, D., Solanki, K., 2010. On kinematic, thermodynamic, and kinetic coupling of a damage theory for polycrystalline material. Int. J. Plast. 26 (6), 775–793. http://dx.doi.org/10.1016/j.ijplas.2009.10.006, URL http://www.sciencedirect.com/science/article/pii/S0749641909001399.

Barbe, F., Decker, L., Jeulin, D., Cailletaud, G., 2001. Intergranular and intragranular behavior of polycrystalline aggregates. Part 1: F.E. model. Int. J. Plast. 17 (4), 513–536. http://dx.doi.org/10.1016/S0749-6419(00)00061-9, URL http://www.sciencedirect.com/science/article/pii/S0749641900000619.

Ben-Boubaker, H., Mareau, C., Ayed, Y., Germain, G., Tidu, A., 2020. Impact of the initial microstructure and the loading conditions on the deformation behavior of the Ti17 titanium alloy. J. Mater. Sci. 55 (4), 1765–1778. http://dx.doi.org/10.1007/s10853-019-04014-5.

Boudifa, M., Saanouni, K., Chaboche, J.-L., 2009. A micromechanical model for inelastic ductile damage prediction in polycrystalline metals for metal forming. Int. J. Mech. Sci. 51 (6), 453–464. http://dx.doi.org/10.1016/j.ijmecsci.2009.03.014.

Boyer, R., Briggs, R., 2005. The use of β titanium alloys in the aerospace industry. J. Mater. Eng. Perform. 14 (6), 681–685.

Bridier, F., McDowell, D.L., Villechaise, P., Mendez, J., 2009. Crystal plasticity modeling of slip activity in Ti–6Al–4V under high cycle fatigue loading. Int. J. Plast. 25 (6), 1066–1082. http://dx.doi.org/10.1016/j.ijplas.2008.08.004, URL http://www.sciencedirect.com/science/article/pii/S0749641908001265.

Bridier, F., Villechaise, P., Mendez, J., 2008. Slip and fatigue crack formation processes in an α/β titanium alloy in relation to crystallographic texture on different scales. Acta Mater. 56 (15), 3951–3962. http://dx.doi.org/10.1016/j.actamat.2008.04.036, URL http://www.sciencedirect.com/science/article/pii/S1359645408002917.

de Buruaga, M.S., Soler, D., no, P.A., Esnaola, J., Arrazola, P., 2018. Determining tool/chip temperatures from thermography measurements in metal cutting. Appl. Therm. Eng. 145, 305–314. http://dx.doi.org/10.1016/j.applthermaleng.2018.09.051, URL https://www.sciencedirect.com/science/article/pii/S1359431118338547.

Cai, J., Wang, K., Han, Y., 2016. A comparative study on Johnson Cook, Modified Zerilli–Armstrong and Arrhenius-type constitutive models to predict high-temperature flow behavior of Ti-6Al-4V alloy in α+ β phase. High Temp. Mater. Process. 35 (3), 297–307.

Cai, J., Wang, K., Zhai, P., Li, F., Yang, J., 2015. A modified Johnson-Cook constitutive equation to predict hot deformation behavior of Ti-6Al-4V alloy. J. Mater. Eng. Perform. 24 (1), 32–44.

Calamaz, M., Coupard, D., Girot, F., 2008. A new material model for 2D numerical simulation of serrated chip formation when machining titanium alloy Ti–6Al–4V. Int. J. Mach. Tools Manuf. 48 (3), 275–288. http://dx.doi.org/10.1016/j.ijmachtools.2007.10.014, URL http://www.sciencedirect.com/science/article/pii/S0890695507002283.

Chaboche, J., 2008. A review of some plasticity and viscoplasticity constitutive theories. Int. J. Plast. 24 (10), 1642–1693. http://dx.doi.org/10.1016/j.ijplas.2008.03.009, URL http://www.sciencedirect.com/science/article/pii/S0749641908000582. Special Issue in Honor of Jean-Louis Chaboche.

Che, J., Zhou, T., Liang, Z., Wu, J., Wang, X., 2018. An integrated Johnson-Cook and Zerilli-Armstrong model for material flow behavior of Ti-6Al-4V at high strain rate and elevated temperature. J. Braz. Soc. Mech. Sci. Eng. 40 (5), 253.

Childs, T.H., Arrazola, P.J., Aristimuno, P., Garay, A., Sacristan, I., 2018. Ti6Al4V Metal cutting chip formation experiments and modelling over a wide range of cutting speeds. J. Mater. Process. Technol. 255, 898–913. http://dx.doi.org/10.1016/j.jmatprotec.2018.01.026, URL http://www.sciencedirect.com/science/article/pii/S092401361830027X.

Dawson, A.L., Blackwell, P., Jones, M., Young, J.M., Duggan, M.A., 1998. Hot rolling and superplastic forming response of net shape processed Ti-6AI-4V produced by centrifugal spray deposition. Mater. Sci. Technol. 14 (7), 640–650. http://dx.doi.org/10.1179/mst.1998.14.7.640, URL DOI: 10.1179/mst.1998.14.7.640.

Farooq, H., Cailletaud, G., Forest, S., Ryckelynck, D., 2020. Crystal plasticity modeling of the cyclic behavior of polycrystalline aggregates under non-symmetric uniaxial loading: Global and local analyses. Int. J. Plast. 126, 102619. http://dx.doi.org/10.1016/j.ijplas.2019.10.007, URL http://www.sciencedirect.com/science/article/pii/S0749641919305108.

Goh, C.H., Neu, R.W., McDowell, D.L., 2003. Crystallographic plasticity in fretting of Ti–6AL–4V. Int. J. Plast. 19 (10), 1627–1650. http://dx.doi.org/10.1016/S0749-6419(02)00039-6, URL http://www.sciencedirect.com/science/article/pii/S0749641902000396.

Guo, B., Semiatin, S., Jonas, J.J., 2019. Dynamic transformation during the high temperature deformation of two-phase titanium alloys. Mater. Sci. Eng.: A 761, 138047. http://dx.doi.org/10.1016/j.msea.2019.138047, URL http://www.sciencedirect.com/science/article/pii/S0921509319308330.

Harzallah, M., Pottier, T., Senatore, J., Mousseigne, M., Germain, G., Landon, Y., 2017. Numerical and experimental investigations of ti-6al-4V chip generation and thermo-mechanical couplings in orthogonal cutting. Int. J. Mech. Sci. 134, 189–202. http://dx.doi.org/10.1016/j.ijmecsci.2017.10.017, URL http://www.sciencedirect.com/science/article/pii/S0020740317308913.

Hill, R., 1967. The essential structure of constitutive laws for metal composites and polycrystals. J. Mech. Phys. Solids 15 (2), 79–95. http://dx.doi.org/10.1016/0022-5096(67)90018-X, URL http://www.sciencedirect.com/science/article/pii/002250966790018X.

Hill, R., 1972. On constitutive macro-variables for heterogeneous solids at finite strain. Proc. R. Soc. Lond. Ser. A. Math. Phys. Sci. 326 (1565), 131–147.

Johnson, G., Cook, W.H., 1983. A constitutive model and data for materials subjected to large strains, high strain rates, and high temperatures. In: Proc. 7th Inf. Sympo. Ballistics, pp. 541–547.

Jovic, C., Wagner, D., Herve, P., Gary, G., Lazzarotto, L., 2006. Mechanical behaviour and temperature measurement during dynamic deformation on split Hopkinson bar of 304L stainless steel and 5754 aluminium alloy. J. Phys. IV France 134, 1279–1285. http://dx.doi.org/10.1051/jp4:2006134194.

Kachanov, L., 1958. Time of the rupture process under creep conditions. Nank SSR Otd Tech Nauk 8, 26–31.

Kalidindi, S., 1998. Incorporation of deformation twinning in crystal plasticity models. J. Mech. Phys. Solids 46 (2), 267–290. http://dx.doi.org/10.1016/S0022-5096(97)00051-3, URL http://www.sciencedirect.com/science/article/pii/S0022509697000513.

Kapoor, K., Noraas, R., Seetharaman, V., Sangid, M., 2019. Modeling strain localization in microtextured regions in a titanium alloy: Ti-6Al-4V. Integrating Mater. Manuf. Innov. 8 (4), 455–467.

Kapoor, K., Ravi, P., Noraas, R., Park, J.S., Venkatesh, V., Sangid, M.D., 2020. Modeling Ti-6Al-4V using crystal plasticity, calibrated with multi-scale experiments, to understand the effect of the orientation and morphology of the α and β phases on time dependent cyclic loading. J. Mech. Phys. Solids 104192. http://dx.doi.org/10.1016/j.jmps.2020.104192, URL http://www.sciencedirect.com/science/article/pii/S0022509620304178.

Kasemer, M., Echlin, M.P., Stinville, J.C., Pollock, T.M., Dawson, P., 2017. On slip initiation in equiaxed α/β Ti-6Al-4V. Acta Mater. 136, 288–302. http://dx.doi.org/10.1016/j.actamat.2017.06.059, URL http://www.sciencedirect.com/science/article/pii/S1359645417305360.

Kim, J., Yoon, J.W., 2015. Necking behavior of AA 6022-T4 based on the crystal plasticity and damage models. Int. J. Plast. 73, 3–23. http://dx.doi.org/10.1016/j.ijplas.2015.06.013, Special Issue on Constitutive Modeling from Micro-Scale to Continuum in Honor of Prof. Frédéric Barlat.

Kolli, R., Devaraj, A., 2018. A review of metastable beta titanium alloys. Metals 8 (7), 506.

Lee, E., 1969. Elastic-plastic deformation at finite strains. J. Appl. Mech. 36 (1), 1–6.

Lee, W.S., Lin, C.F., 1998. Plastic deformation and fracture behaviour of Ti–6Al–4V alloy loaded with high strain rate under various temperatures. Mater. Sci. Eng.: A 241 (1), 48–59. http://dx.doi.org/10.1016/S0921-5093(97)00471-1, URL http://www.sciencedirect.com/science/article/pii/S0921509397004711.

Lemaitre, J., Chaboche, J., Benallal, A., Desmorat, R., 1985. Mécanique des matériaux Solides-1^{ere} édition. Dunod.

Lewis, A.C., Qidwai, S.M., Geltmacher, A.B., 2010. Slip systems and initiation of plasticity in a body-centered-cubic titanium alloy. Metall. Mater. Trans. 41 (10), 2522–2531. http://dx.doi.org/10.1007/s11661-010-0284-5.

Lhadi, S., Berbenni, S., Gey, N., Richeton, T., Germain, L., 2018. Micromechanical modeling of the effect of elastic and plastic anisotropies on the mechanical behavior of β-Ti alloys. Int. J. Plast. 109, 88–107. http://dx.doi.org/10.1016/j.ijplas.2018.05.010, URL http://www.sciencedirect.com/science/article/pii/S0749641918301839.

Li, L., Peng, D., Liu, J., Liu, Z., 2001. An experiment study of the lubrication behavior of graphite in hot compression tests of Ti–6Al–4V alloy. J. Mater. Process. Technol. 112 (1), 1–5. http://dx.doi.org/10.1016/S0924-0136(00)00845-1, URL http://www.sciencedirect.com/science/article/pii/S0924013600008451.

Liang, R., Khan, A.S., 1999. A critical review of experimental results and constitutive models for BCC and FCC metals over a wide range of strain rates and temperatures. Int. J. Plast. 15 (9), 963–980. http://dx.doi.org/10.1016/S0749-6419(99)00021-2, URL http://www.sciencedirect.com/science/article/pii/S0749641999000212.

Lindroos, M., Laukkanen, A., Andersson, T., Vaara, J., Mantyla, A., Frondelius, T., 2019. Micromechanical modeling of short crack nucleation and growth in high cycle fatigue of martensitic microstructures. Comput. Mater. Sci. 170, http://dx.doi.org/10.1016/j.commatsci.2019.109185.

Ling, C., Besson, J., Forest, S., Tanguy, B., Latourte, F., Bosso, E., 2016. An elasto-viscoplastic model for porous single crystals at finite strains and its assessment based on unit cell simulations. Int. J. Plast. 84, 58–87. http://dx.doi.org/10.1016/j.ijplas.2016.05.001, URL https://www.sciencedirect.com/science/article/pii/S0749641916300699.

Mandel, J., 1973. Equations constitutives et directeurs dans les milieux plastiques et viscoplastiques. Int. J. Solids Struct. 9 (6), 725–740.

Mareau, C., 2020. A non-local damage model for the fatigue behaviour of metallic polycrystals. Phil. Mag. 100 (8), 955–981. http://dx.doi.org/10.1080/14786435.2020.1713412.

Marigo, J.-J., 1991. Formulation d'une loi d'endommagement d'un matériau élastique. C. R. Acad. Sci. Paris 292, 1309–1312.

Martin, G., Ochoa, N., Saï, K., Hervé-Luanco, E., Cailletaud, G., 2014. A multiscale model for the elastoviscoplastic behavior of Directionally Solidified alloys: Application to FE structural computations. Int. J. Solids Struct. 51 (5), 1175–1187. http://dx.doi.org/10.1016/j.ijsolstr.2013.12.013, URL http://www.sciencedirect.com/science/article/pii/S0020768313004861.

Mecking, H., Kocks, U., 1981. Kinetics of flow and strain-hardening. Acta Metall. 29 (11), 1865–1875. http://dx.doi.org/10.1016/0001-6160(81)90112-7, URL http://www.sciencedirect.com/science/article/pii/0001616081901127.

Momeni, A., Abbasi, S., 2010. Effect of hot working on flow behavior of Ti–6Al–4V alloy in single phase and two phase regions. Mater. Des. 31 (8), 3599–3604. http://dx.doi.org/10.1016/j.matdes.2010.01.060, URL http://www.sciencedirect.com/science/article/pii/S0261306910001354.

Nemat-Nasser, S., Lori, M., Datta, S., 1996. Micromechanics: overall properties of heterogeneous materials.

Orlans-Joliet, B., Bacroix, B., Montheillet, F., Driver, J., Jonas, J., 1988. Yield surfaces of b.c.c. crystals for slip on the ⟨111⟩ {110} and ⟨111⟩ {112} systems. Acta Metall. 36 (5), 1365–1380. http://dx.doi.org/10.1016/0001-6160(88)90288-X, URL http://www.sciencedirect.com/science/article/pii/000161608890288X.

Quey, R., Dawson, P., Barbe, F., 2011. Large-scale 3D random polycrystals for the finite element method: Generation, meshing and remeshing. Comput. Methods Appl. Mech. Engrg. 200 (17), 1729–1745. http://dx.doi.org/10.1016/j.cma.2011.01.002, URL http://www.sciencedirect.com/science/article/pii/S004578251100003X.

Roters, F., Eisenlohr, P., Hantcherli, L., Tjahjanto, D., Bieler, T., Raabe, D., 2010. Overview of constitutive laws, kinematics, homogenization and multiscale methods in crystal plasticity finite-element modeling: Theory, experiments, applications. Acta Mater. 58 (4), 1152–1211. http://dx.doi.org/10.1016/j.actamat.2009.10.058, URL http://www.sciencedirect.com/science/article/pii/S1359645409007617.

Sabnis, P.A., Forest, S., Cormier, J., 2016. Microdamage modelling of crack initiation and propagation in FCC single crystals under complex loading conditions. Comput. Methods Appl. Mech. Engrg. 312, 468–491.

Salem, A., Kalidindi, S., Semiatin, S., 2005. Strain hardening due to deformation twinning in α-titanium: Constitutive relations and crystal-plasticity modeling. Acta Mater. 53 (12), 3495–3502. http://dx.doi.org/10.1016/j.actamat.2005.04.014, URL http://www.sciencedirect.com/science/article/pii/S1359645405002168.

Salib, M., Teixeira, J., Germain, L., Lamielle, E., Gey, N., Aeby-Gautier, E., 2013. Influence of transformation temperature on microtexture formation associated with α precipitation at β grain boundaries in a β metastable titanium alloy. Acta Mater. 61 (10), 3758–3768. http://dx.doi.org/10.1016/j.actamat.2013.03.007, URL http://www.sciencedirect.com/science/article/pii/S1359645413002036.

Scherer, J.-M., Besson, J., Forest, S., Hure, J., Tanguy, B., 2021. A strain gradient plasticity model of porous single crystal ductile fracture. J. Mech. Phys. Solids 156, 104606. http://dx.doi.org/10.1016/j.jmps.2021.104606.

Semiatin, S., Seetharaman, V., Ghosh, A., 1999. Plastic flow, microstructure evolution, and defect formation during primary hot working of titanium and titanium aluminide alloys with lamellar colony microstructures. Philos. Trans. R. Soc. Lond. Ser. A Math. Phys. Eng. Sci. 357 (1756), 1487–1512.

Sima, M., Ozel, T., 2010. Modified material constitutive models for serrated chip formation simulations and experimental validation in machining of titanium alloy Ti–6Al–4V. Int. J. Mach. Tool. Manuf. 50 (11), 943–960. http://dx.doi.org/10.1016/j.ijmachtools.2010.08.004, URL http://www.sciencedirect.com/science/article/pii/S0890695510001446.

Suiker, A., Turteltaub, S., 2005. Computational modelling of plasticity induced by martensitic phase transformations. Internat. J. Numer. Methods Engrg. 63 (12), 1655–1693. http://dx.doi.org/10.1002/nme.1327.

Teixeira, J., Appolaire, B., Aeby-Gautier, E., Denis, S., Bruneseaux, F., 2006. Modeling of the effect of the β phase deformation on the α phase precipitation in near-β titanium alloys. Acta Mater. 54 (16), 4261–4271. http://dx.doi.org/10.1016/j.actamat.2006.05.019, URL http://www.sciencedirect.com/science/article/pii/S1359645406003569.

Teixeira, J., Appolaire, B., Aeby-Gautier, E., Denis, S., Cailletaud, G., Spath, N., 2007. Transformation kinetics and microstructures of Ti17 titanium alloy during continuous cooling. Mater. Sci. Eng.: A 448 (1), 135–145. http://dx.doi.org/10.1016/j.msea.2006.10.024.

Thimm, B., Glavas, A., Reuber, M., Christ, H.-J., 2021. Determination of chip speed and shear strain rate in primary shear zone using digital image correlation (DIC) in linear-orthogonal cutting experiments. J. Mater. Process. Technol. 289, 116957. http://dx.doi.org/10.1016/j.jmatprotec.2020.116957, URL https://www.sciencedirect.com/science/article/pii/S0924013620303745.

Trabelsi, S., Morel, A., Germain, G., Bouaziz, Z., 2017. Tool wear and cutting forces under cryogenic machining of titanium alloy (Ti17). Int. J. Adv. Manuf. Technol. 91 (5–8), 1493–1505.

Turteltaub, S., Suiker, A., 2006. A multiscale thermomechanical model for cubic to tetragonal martensitic phase transformations. Int. J. Solids Struct. 43 (14), 4509–4545. http://dx.doi.org/10.1016/j.ijsolstr.2005.06.065, URL http://www.sciencedirect.com/science/article/pii/S0020768305003574.

Voigt, W., 1889. Ueber die Beziehung zwischen den beiden Elasticitätsconstanten isotroper Körper. Annalen Der Physik 274 (12), 573–587. http://dx.doi.org/10.1002/andp.18892741206.

Wagner, V., Harzallah, M., Baili, M., Dessein, G., Lallement, D., 2020. Experimental and numerical investigations of the heating influence on the Ti5553 titanium alloy machinability. J. Manuf. Process. 58, 606–614. http://dx.doi.org/10.1016/j.jmapro.2020.08.018, URL http://www.sciencedirect.com/science/article/pii/S1526612520305223.

Weiss, I., Semiatin, S., 1998. Thermomechanical processing of beta titanium alloys—an overview. Mater. Sci. Eng.: A 243 (1), 46–65. http://dx.doi.org/10.1016/S0921-5093(97)00783-1, URL http://www.sciencedirect.com/science/article/pii/S0921509397007831.

Weiss, I., Semiatin, S., 1999. Thermomechanical processing of alpha titanium alloys—an overview. Mater. Sci. Eng.: A 263 (2), 243–256. http://dx.doi.org/10.1016/S0921-5093(98)01155-1, URL http://www.sciencedirect.com/science/article/pii/S0921509398011551.

Wu, H., To, S., 2015. Serrated chip formation and their adiabatic analysis by using the constitutive model of titanium alloy in high speed cutting. J. Alloys Compd. 629, 368–373. http://dx.doi.org/10.1016/j.jallcom.2014.12.230, URL http://www.sciencedirect.com/science/article/pii/S0925838815000250.

Yaich, M., Ayed, Y., Bouaziz, Z., Germain, G., 2017. Numerical analysis of constitutive coefficients effects on FE simulation of the 2D orthogonal cutting process: application to the Ti6Al4V. Int. J. Adv. Manuf. Technol. 93 (1–4), 283–303.

Ye, G., Xue, S., Jiang, M., Tong, X., Dai, L., 2013. Modeling periodic adiabatic shear band evolution during high speed machining Ti-6Al-4V alloy. Int. J. Plast. 40, 39–55. http://dx.doi.org/10.1016/j.ijplas.2012.07.001, URL http://www.sciencedirect.com/science/article/pii/S0749641912001039.

Zaera, R., guez Martí nez, J.R., Rittel, D., 2013. On the Taylor–Quinney coefficient in dynamically phase transforming materials. Application to 304 stainless steel. Int. J. Plast. 40, 185–201. http://dx.doi.org/10.1016/j.ijplas.2012.08.003, URL https://www.sciencedirect.com/science/article/pii/S0749641912001192.

Zerilli, F.J., Armstrong, R.W., 1987. Dislocation-mechanics-based constitutive relations for material dynamics calculations. J. Appl. Phys. 61 (5), 1816–1825.

Zhan, H., Wang, G., Kent, D., Dargusch, M., 2014. Constitutive modelling of the flow behaviour of a β titanium alloy at high strain rates and elevated temperatures using the Johnson–Cook and modified Zerilli–Armstrong models. Mater. Sci. Eng.: A 612, 71–79. http://dx.doi.org/10.1016/j.msea.2014.06.030, URL http://www.sciencedirect.com/science/article/pii/S092150931400745X.

Zhang, Z., Jun, T.S., Britton, T.B., Dunne, F.P., 2016. Determination of Ti-6242 α and β slip properties using micro-pillar test and computational crystal plasticity. J. Mech. Phys. Solids 95, 393–410. http://dx.doi.org/10.1016/j.jmps.2016.06.007, URL http://www.sciencedirect.com/science/article/pii/S0022509616302307.

Zhang, M., Zhang, J., McDowell, D., 2007. Microstructure-based crystal plasticity modeling of cyclic deformation of Ti–6Al–4V. Int. J. Plast. 23 (8), 1328–1348. http://dx.doi.org/10.1016/j.ijplas.2006.11.009, URL http://www.sciencedirect.com/science/article/pii/S0749641906001616.

Zhou, J., Ren, J., Jiang, Y., 2020. Inverse identification of modified Johnson–Cook model for cutting titanium alloy Ti6Al4V using firefly algorithm. Proc. Inst. Mech. Eng., Part B: J. Eng. Manuf. 234 (3), 584–599. http://dx.doi.org/10.1177/0954405419864003.